Optimization of charge curve for the extreme inhibition of growing microstructures during electrodeposition

Asghar Aryanfar*, Yara Ghamlouche, and William A. Goddard III

The formation of branched microstructures during the electrodeposition is a catastrophic event, which hampers the safe utilization of the metallic electrodes in rechargeable batteries. Focusing on the nonlinear growth dynamics of the dendritic microstructures, we tune the rate of the feeding charge against their growth pace to minimize the amount of the dendritic branching, while maintaining a constant feeding charge. The ultimate morphology of the electrodeposits has been shown to be more compact than the conventional uniform charging in terms of the density of the electrodeposits. Due to analytical derivation and the coupled development of the optimal charge form with respect to the natural kinetics of dendritic evolution in real time, we infer that it prevents the branching of the electrodeposits to the greatest extent, during the stochastic evolution of the dendrites.

Impact statement

Taking into account the runaway behavior in the natural growth rate of the dendritic electrodeposition, which is slowest in the initiation (i.e., triggering) stage and is fastest in the final (i.e., short circuit) stage, we tune the rate of the feeding charge in time, inversely for highest compression of the microstructures, while maintaining a constant total charge. The controlled dendritic growth with the constant speed has analytically been proven to lead to the shortest growth compared with any other runaway growth form, while maintaining the same amount of the total charge. Subsequently, the constant rate of growth has been used as the handle to obtain the charge feeding form leading to such rate of growth. Performing stochastic molecular dynamics (MD) simulations, the ultimate morphology of the electrodeposits has been shown to be more compact than the conventional uniform charging in terms of the density of the electrodeposits. In fact, the charge feeding occurs when the density of the growing structure is the highest, and vice versa, the feeding rate is the least, when the structure is the most branched and sparse. The obtained charging protocol has been successfully tested in our experimental observations, which has visually led to the shorter accumulation of the dendrites with higher packing density. Due to analytical derivation and comparative development of the optimal pulse form with respect to the natural kinetics of dendritic evolution, we infer that it prevents the branching of the electrodeposits almost to the greatest extent, during the stochastic evolution of the dendrites.

Introduction

Portable energy sources are at the heart of new technologies and modern devices essential for the daily life, such as electronic devices, electric vehicles, and power banks, among many other applications. An important source of energy for such applications is high energy density rechargeable batteries.[1] Lithium-based batteries are considered high energy density batteries possessing unique characteristics that explain their wide and continuous use in modern applications.[2,3] These favorable features include high-specific capacity and low-redox potential.[4] Nevertheless, there are certain limitations of their use due to certain properties that need to be addressed. One of these unpleasant properties is the branched dendritic growth of the atoms. During the disposition of the ions, their high reactivity causes the atoms to form branched surfaces that result in a majorly hollow medium of microstructures instead of disposing into a smooth surface and a resulting dense medium.[5,6] This type of growth allows the atoms to perforate the separator and cause short-circuiting, which leads to undesirable and dangerous consequences.[7–9] Additionally, they can also dissolve from their thinner necks during subsequent discharge period and form detached dead crystals, which leads to thermal instability and capacity decay.[10] These problems present a crucial ongoing complication for the utilization of rechargeable metal-based batteries.[11,12] The necessity for methods leading to the dendrites suppression and the formation of a packed medium is therefore a priority.

Asghar Aryanfar, American University of Beirut, Lebanon; Bahçeşehir University, Turkey; aryanfar@caltech.edu
Yara Ghamlouche, American University of Beirut, Lebanon
William A. Goddard III, California Institute of Technology, USA
*Corresponding author

doi:10.1557/s43577-022-00307-4

Earlier efforts have focued on the morphological growth of atoms based on the diffusion-limited aggregation (DLA) of particles,[13–15] whereas the later models established the space charge and electric field[16–18] as the drive for dendritic growth; and the more recent studies shifted toward concentration-based modeling.[19,20] These factors partially contribute to the electrochemical potential. However, the ultimate morphology depends on the localization and dominance of electric potential and the ionic concentration.[21] Contemporary studies have investigated their interchangeable roles in the continuum scale and in coarse–time intervals, reaching to the scale of the experiments in time and space.[22] Others include phase-field modeling[23–25] and Arrhenius-type development.[26] The most recent approaches toward this problem investigated mechanical suppression with solid–solid interfaces,[27] placement of the Li ions in a scaffold,[2,28,29] a variety of coating material,[11] and usage of additives.[4,30,31]

The Brownian motion of the ions during the electrodeposition and the nonuniform morphology of the electrode's surface are the main reasons behind the branched growth of the dendrites.[32] When ions are deposited, their shape on the deposited surface creates a form of surface sharpness. The latter possesses a large electric field, which attracts more ions as an electrodeposition sink. More ions are thus deposited and accumulated on the same sharp edges of the surface making them even sharper each time. As the charge–discharge cycle continues, the dendritic growth exacerbates further. Regardless of their high porosity, the growing amorphous crystals have considerable strength and could pierce into the polymer electrolyte and shorten the cell.[33]

Current research in the field has touched on different factors affecting the dendritic growth such as the current density,[34,35] the solvent and electrolyte chemical composition,[36–38] the roughness of the electrode surface,[39,40] temperature,[41–43] cathode morphology,[44] pulse charging,[45,46] external pressure and deformation,[47,48] and mechanics.[49–51] The characterization methods include NMR[52] and MRI.[53] Furthermore, some work has focused on the stability of the solid–electrolyte interphase (SEI) for controlling the development of the branched medium.[54–56]

Among the different approaches used to suppress dendrites formation, the pulse method has lately been proven to be effective.[22,57] The reduction reactions that causes ions depletion, alongside the mass flux to and away from a certain region have a collaborative job in determining the concentration of ions in a given region. While the reaction pattern is stochastic for all types of surfaces, the sharp edges represent high-electric-field zones, and therefore, highly manipulate the ionic influx,[58] leading to the undesirable attachment of the ions on the tips during the charging period. The significance of the subsequent rest period would be to diffuse ions away toward the less concentrated zones,[59] which leads to the formation of a more uniform morphology during the coming charging period. In previous works, we have computationally adjusted such period based on the radius of curvature of the sharpest tip[60] and we have investigated the role of pulse-reverse protocol on removal of sharp dendritic branches.[58]

In this study, we base our model on natural dynamics of the evolution of microstructure to change the form of the feeding charge rate that could result in decreasing the micro-structural dendritic morphology. To compress the dendrites, we supply a slower feeding charge rate during the faster pace of natural dendritic growth by means of analytical development. Afterward, the method is tested against the uniform charging both numerically and experimentally where the computational method consists of coarse grain modeling and the experimental method includes the optical observation and measurement analysis.

Methodology

The general layout of dendritic growth is represented schematically in **Figure 1**a. The morphology of the electrodeposits highly depends on the movement pattern of the ions. Such motion is typically a factor of the electric field as well as the diffusion in the electrolytic medium. While the former is a majorly vertical displacement from the high electric field in the tips (i.e., vector M) causing the accelerated formation of branched dendrites (unfavorable), the latter causes sidewise movement (i.e., vector D), leading to simultaneous uniformization and shaping more packed medium (favorable). Additionally, such morphology is highly sensitive to the feeding rate, which correlates with the voltage V. Three candidates of charging forms are illustrated in Figure 1b.

Natural evolution of the microstructures

To obtain the optimized form of the feeding charge rate for the largest suppression of the dendrites, one needs to understand the real-time pattern of the dendrite growth. While the ionic diffusion occurs in all directions, the migration of ions from electric field is solely toward the tips of the dendrites. Due to the significantly high amount of the electric field E in the vicinity of those sites,[22] the rate of growth is mainly driven by electro-migration, particularly for high-voltage and low-concentration applications. During the coarse–scale time interval $\mathrm{d}t$, which extends beyond the double layer and into the electrolyte of the ambient concentration C_∞, the approaching ions with the drift velocity of μE will increase the tip elevation by $d\lambda$, which is inversely proportional to the spatial density of microstructure ρ_{ave} as:

$$d\lambda = \frac{\Omega C_\infty}{\rho_{\mathrm{ave}}} \mu E \mathrm{d}t, \tag{1}$$

where Ω and μ are the molar volume and the mobility of the upcoming ions, respectively, E is the electric field, which depends on the inter-electrode distance (i.e., $E = \frac{\bar{V}}{d}$) and is also augmented due to the dendrite radius of the curvature r_{d}. Thus, during the infinitesimal time interval $\mathrm{d}t$ one has:

$$E = f(r_{\mathrm{d}}) \frac{\Delta V}{l - \lambda}, \tag{2}$$

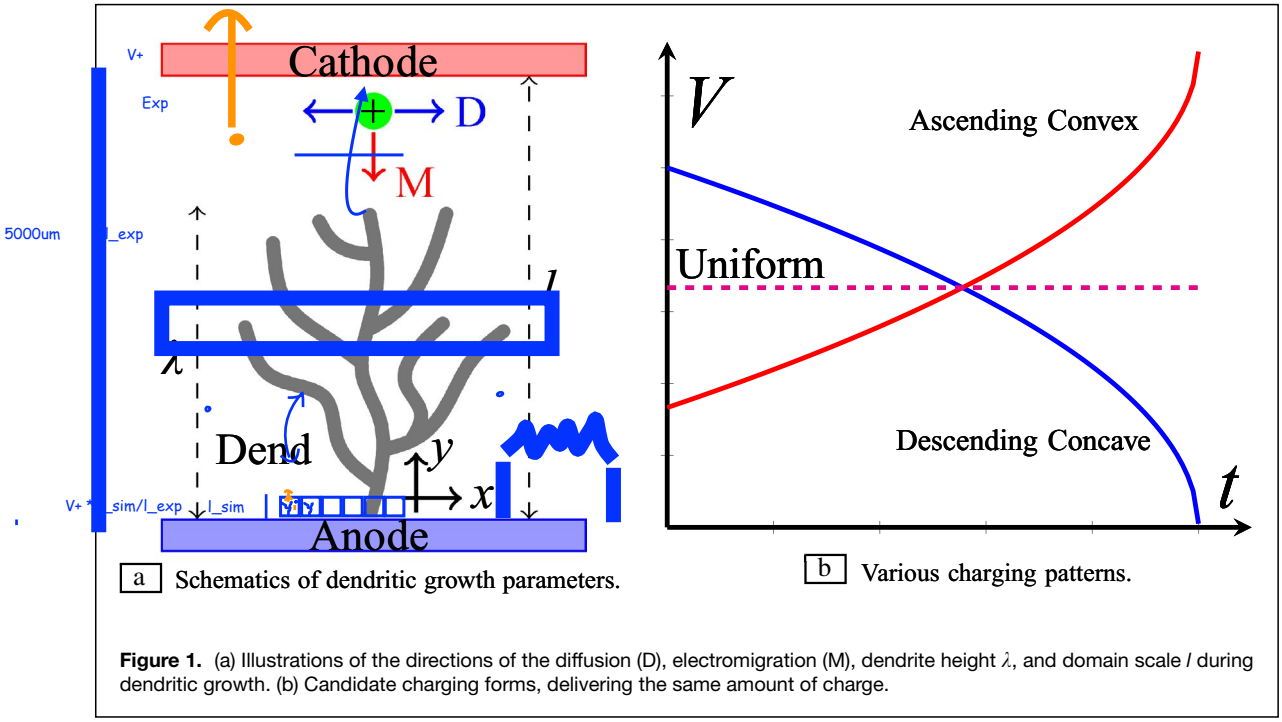

Figure 1. (a) Illustrations of the directions of the diffusion (D), electromigration (M), dendrite height λ, and domain scale l during dendritic growth. (b) Candidate charging forms, delivering the same amount of charge.

where $f(r_d)$ is the curvature scaling value due to geometry of the interface, $\bar{V}$ is the inter-electrode potential difference, l is the inter-electrode distance. The previous equation is integrable as follows:

$$\int_0^{\lambda}(l-\lambda)\mathrm{d}\lambda = \frac{\Omega C_{\infty}}{\rho_{ave}}\mu f(r_d)\Delta V\int_0^{t}\mathrm{d}t. \tag{3}$$

We define the parameter $\mu_d := \frac{\Omega C_{\infty}}{\rho_{ave}}\mu f(r_d)$, which possesses the unit of $m^2\,V^{-1}\,s^{-1}$ and thus is an indicator of the mobility of the evolving dendrites. Re-arranging and integrating yields:

$$\lambda^2 - 2l\lambda + 2\mu_d\Delta V t = 0. \tag{4}$$

Assuming that the inter-electrode voltage ΔV is constant, one can solve the previous parabolic relationship:

$$\lambda = l - \sqrt{l^2 - 4\mu_d\Delta V t}. \tag{5}$$

Subsequently, the rate of growth is obtained as:

$$\dot{\lambda} = \frac{2\mu_d\Delta V}{\sqrt{l^2 - 4\mu_d\Delta V t}}, \tag{6}$$

which describes the dendritic height λ as a function of time t. The short-circuit time can also be obtained by setting $\lambda := l$ as follows:

$$t_{short} = \frac{l^2}{4\mu_d\Delta V}. \tag{7}$$

Figures 2a and 2b shows the state and rate of evolution of the microstructure based on the parameters given in **Table** I. The mobility μ in this table is obtained via the Einstein relationship as:

$$\mu = \frac{De}{k_B T} = \frac{2.6\times10^{-10}\times1.6\times10^{-19}}{1.38\times10^{-23}\times298} \approx 10^{-8}\frac{m^2}{V.s}. \tag{8}$$

Additionally, the reported voltage difference ΔV and inter-electrode distance l are set as the standard values for the conventional lithium-ion batteries. The scaling factor $f(r_d)$ is assumed based on the natural concave form (i.e., curvature) of the interface. During the initial stages of growth, the microstructures have high spatial density ($\rho \to 1$), while later on they become disconnected and tend to be more sparse, particularly on the verge of short-circuit ($\rho \to 0$). Hence, the assumed average value for the dense electrodeposits (i.e., $\rho_{ave} \approx 0.5$), which represents the organized pattern of the growth morphology.

Controlled evolution

It is evident from the growth trend in Equation 5 that the dendrite growth has an accelerating behavior. For the constant amount of charge, due to quickening nature of the growth, the higher charge-feeding rate in a certain period of time is more costly for growing the dendrites, albeit causing the lower feeding rate in other time intervals. Since the natural growth pattern is monotonous and the curvature of the growth rate in Figure 2b is positive, hence:

$$\frac{\mathrm{d}^2\dot{\lambda}}{\mathrm{d}t^2} > 0; \tag{9}$$

the implication of this equation in the infinitesimal time interval δt would be:

$$\dot{\lambda}(t+\delta t) + \dot{\lambda}(t-\delta t) > 2\dot{\lambda}.$$

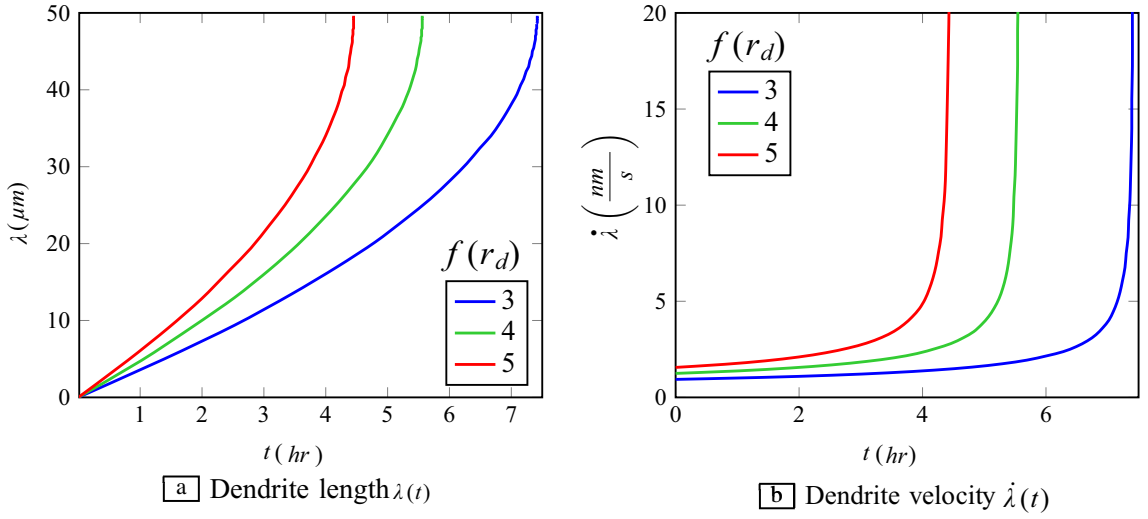

Figure 2. The natural evolution of the dendrite height λ (a) and its respective growing velocity $\dot{\lambda}$ (b) during electrodeposition.

Table I. The parameters for analytical development.

Parameter	Value	Unit	References
Ω	13×10^{-6}	$m^3\ mol^{-1}$	61
D	2.6×10^{-10}	$m^2\ s^{-1}$	62
C_∞	1	$mol\ m^{-3}$	16
ΔV	3	V	63
l	25×10^{-6}	m	63
k_B	1.38×10^{-23}	$J\ K^{-1}$	64
e	1.6×10^{-19}	C	64
$f(r_d)$	{3, 4, 5}	[ ]	Assumed (range)
ρ_{ave}	0.5	[ ]	Average value

Therefore, the growth rate is obtained as:

$$\int \dot{\lambda}(t+\delta t)\mathrm{d}t + \int \dot{\lambda}(t-\delta t)\mathrm{d}t > 2\int \dot{\lambda}\mathrm{d}t, \tag{10}$$

which means that for any perturbation in the rate of growth, the eventual grown value will be higher and hence the best case scenario for the minimization of the dendrite is the ultimate *steady-state* and *controlled* growth regime with the velocity of $\dot{\lambda}_{cont}$.

$$\dot{\lambda}_{cont} = \int_0^{\frac{l^2}{4\mu_d \Delta V}} \ddot{\lambda}\mathrm{d}t = \frac{4\mu_d \Delta V}{l} \tag{11}$$

Therefore, for an accelerating growth pattern of the dendrites, one needs to apply decelerating charge pattern in order to get a uniform growth speed. One needs to get the rate of evolution of the dendrites in Equation 6 with the new assigned voltage pattern V_{OPT} and the average rate of growth in Equation 11. Hence, the rate of growth should follow:

$$\frac{2\mu_d V_{OPT}}{\sqrt{l^2 - 4\mu_d V_{OPT} t}} = \frac{4\mu_d \Delta V}{l}. \tag{12}$$

Note that ΔV and V_{OPT} are parameters for two separate charging scenarios where the former is for default constant-voltage charging and the latter is for the new optimized voltage pattern. Simplifying further, we obtain the following quadratic equation:

$$V_{OPT}^2 + \beta t V_{OPT} - 4\Delta V^2 = 0, \tag{13}$$

where $\beta := \frac{16\Delta V^2}{l^2}\mu_d$ and therefore, the solution finally would be:

$$V_{OPT} = \sqrt{\beta^2 t^2 + 16\Delta V^2} - \beta t, \tag{14}$$

which is the optimized voltage pattern to obtain uniformly growing microstructures with the velocity of $\dot{\lambda}_{cont}$. Although based on Equation 12, the new voltage pattern V_{OPT} analytically leads to the same length of the dendrites, however, the stochastic and accelerating nature of the growth, which is not captured in the analytical method, will lead to higher amount of the dendrites. This will be illustrated and justified in the numerical simulation (i.e., next section). The form of the optimized voltage pattern V_{OPT} is illustrated in **Figure 3**a and the corresponding average rate of growth $\dot{\lambda}_{cont}$ is shown in Figure 3b.

Numerical simulations

Typically, the electrodeposition is driven by either the concentration gradient (∇C) or the variation in the electric potential (∇V). In the larger scale of time, the ionic displacements are approximated by the diffusion length. Nevertheless, the ions will acquire a drift velocity within the the electric field of the

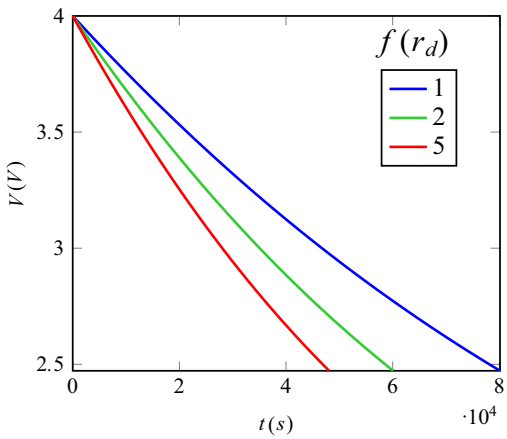

a The obtained optimal voltage form versus time for different curvature scaling values $f(r_d)$.

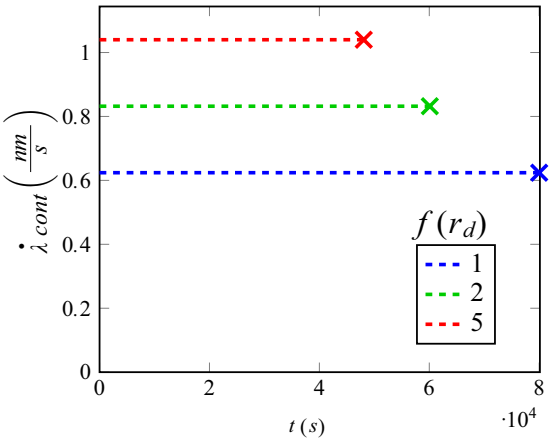

b The resulted uniformly growing velocities $\dot{\lambda}_{cont}(t)$ in time for different curvature scaling values $f(r_d)$.

Figure 3. The attained optimal voltage $V(t)$ form with the obtained respective growing velocity $\dot{\lambda}(t)$.

electrolyte medium. Hence, the total displacement of the ions for the interval of δt is given by References 22 and 65:*

$$\delta\vec{\mathbf{r}} = \sqrt{2D^{+}\delta t}\,\hat{\mathbf{g}} + \mu^{+}\vec{\mathbf{E}}\delta t, \tag{15}$$

where D^+ is the ionic diffusion coefficient, and $\hat{\mathbf{g}}$ is a normalized vector in a random direction, representing the Brownian dynamics, μ^+ is the mobility of cations in electrolyte, $\vec{\mathbf{E}}$ is the local electric field, which represents the gradient of electric potential ($\vec{\mathbf{E}} = -\nabla V$). The diffusion length represents the average progress of a diffusive wave in a given time, obtained directly from the diffusion equation.[66]

The voltage profile V is calculated using Gauss' Law and assuming electro-neutrality in the electrolytic domain[67] with the dendrite's voltage being the same as the electrode's, since they are physically connected. The numerical method has been applied to both the uniform and the optimal charging protocols based on the parameters given in **Table II** and adopting the diffusivity and voltage values of Table I. The resulted morphologies are presented in **Figure 4**, where the red aggregates are the grown dendrites, blue particles are the free ions, the green vectors are the electric field and the dashed curve is the approximate location of the interface, corresponding to the area where the computed voltage approaches the voltage of dendrites.

As shown in **Figure 5**, each curve has been discretized to multiple infinitesimal uniform charges. Each of these rectangles represents a certain deposited charge number. **Table III** shows an example for such segmentation. While the uniform method deposits identical number of atoms during the charge period, the optimal form follows a decreasing trend during the electrodeposition. A negligible rest period is applied between each subsequent deposition to differentiate the charge amount between each time segmentation. During the charging period both migration and diffusion are in action, whereas the diffusion is the only driving mechanism throughout the relaxation period. Although during this relaxation period the atoms diffuse from their positions to lower concentrated areas, however such period has similar effect on both uniform and optimal charging patterns. After the last deposition, a longer rest period is supplied to the system after which the process restarts all over again. The process continues until the maximum number of deposited atoms is reached.

The resulting densities are presented in **Figure 6** based on the number of deposited atoms and the latest point in each line shows the short circuit location. To decrease the randomness effect in the values, each point is computed as the average of four separate simulation runs.

Experimental

We have performed experiments within manually fabricated sandwich cells[68] that provide the possibility of *in situ* observation of the growing dendrites from their outer boundaries (**Figure 7**a). The cell consists of two circular Li^0 electrodes with the diameters of 1.59 cm ($D = 7.95$ cm) and the inter-electrode distance of $L = 0.32$ cm (i.e., $\frac{1}{8}''$) via a transparent acrylic PMMA (i.e., plexiglass) separator/housing. The fabricated cells were filled via syringe with 0.4 cm^3 of $LiPF_6$ in the solvent with the volumetric proportions of EC:EMC ≡ 1:1 in an argon-filled glovebox ($H_2O, O_2 < 0.5$ ppm). Multiple such cells were charged the passage of the variable charge of $Q = \{12, 24, 48\}$ mAh** and based on the parameters given in **Table IV**, generated by a

* $\delta t = \sum_{i=1}^{n} \delta t_i$ where δt_k is the inter-collision time, typically in the range of *fs*.

** Equivalent to $Q \approx \{43, 86, 174\}$ coulombs.

Table II. Simulation parameters.

Var.	Value	References
Domain size	$16.7 \times 16.7\ \text{nm}^2$	22
δt (μs)	10	Assumed
#Li^+	200	Assumed
#Li^0	400	Assumed

programmable multichannel SP150 Bio-Logic potentiostat. After each experiment, three images were taken from the periphery of 120^0 by means of Leica M205FA optical microscope through the acrylic separator. The image processing algorithm is subsequently established as:

1. The RGB image is inserted into the program with the three color values of $\{R, G, B\} \in [0, 255]$ and has been extracted and normalized to a grayscale intensity image I with individual values of range $I_{i,j} \in [0, 1]$.
2. The grayscale image $I_{i,j}$ is binarized into $J_{i,j}$ via the grayness threshold I_c such that:

$$J_{i,j} = \begin{cases} 1 & I_{i,j} \geq I_c \\ 0 & I_{i,j} < I_c \end{cases}$$

the threshold value I_c has been chosen to minimize the weighted intra-class variance σ^2 defined proportionally as:

$$\begin{cases} \sigma^2 = \omega_0\sigma_0^2 + \omega_1\sigma_1^2 \\ \omega_0 + \omega_1 = 1 \end{cases},$$

where ω_0 and ω_1 are the individual weight of each portion as the fraction of total, divided by the value of I_c and σ_0^2 and σ_1^2 are their respective variances.[69] Such minimization ensures that the resulted binary medium of black and white pixels individually fall to the closest proximity of each other, when counted in the same group (i.e., closest ~ lowest variance).

3. The circular sandwich cell with the diameter D has been divided to 3 equal arcs with the angle of $\frac{2\pi}{3}$ (120°) and the width incremental length of δx, which is supposed to be projected to a 2D plane with the incremental width of δs. From the circular geometry in the circle we get: $s = \frac{D}{2}\sin(\theta)$, $\rightarrow$ $\mathrm{d}s = \frac{D}{2}\cos(\theta)\mathrm{d}\theta$, where $\cos(\theta) = \sqrt{1 - \frac{4x^2}{D^2}}$; hence:[70]

$$\delta s = \frac{\delta x}{\sqrt{1 - \frac{4x^2}{D^2}}}.$$

4. Starting from the electrode surface, each individual the occupied space in the distance δx were identified visually and measured by AutoCAD.
5. The infinitesimal calculations have been normalized to inter-electrode distance ($\hat{\lambda}_i := \lambda_i / l$) and integrated to get the average dendrite measure $\hat{\lambda}$ as:

$$\begin{aligned} \hat{\lambda} &= \frac{1}{\pi DL}\sum_{k=1}^{3}\int_{-\frac{\pi}{3}}^{+\frac{\pi}{3}} \hat{\lambda}_k(\theta)\frac{D}{2}\mathrm{d}\theta \\ &= \frac{1}{\pi DL}\sum_{k=1}^{3}\int_{-\frac{b}{2}}^{+\frac{b}{2}} \frac{\hat{\lambda}_k(x)\mathrm{d}x}{\sqrt{1 - \frac{4x^2}{D^2}}} \end{aligned}. \tag{16}$$

The integral equation 16 has been obtained by incremental sum from experimental data. Figure 7b shows such investigation for the dendritic formation via uniform charging (top) and the optimal charging (bottom), where the red encirclement is the approximated dendrite area, the green rectangle is the total area, and the dashed line represents the height of the tallest dendrite in each experiment. The optimal charging here has been approximated with the triangular charging curve, which linearly is reduced from the maximum value of 2 mA cm^{-2} to the minimum value of 0. The detailed experimental parameters are given in Table IV. Note that the current density i and the ionic flux j are correlated with $i = zFj$, where z is the valence number of charge carriers and $F = 96.5\ \text{kC mol}^{-1}$ is the Faraday's constant, representing the amount of charge per mole.

Results and discussion

The accelerated growth dynamics of the dendrites, which is shown in Figure 2a–b could get tuned to the uniform growth rate since it leads to the least amount of branching, as shown in Equation 10. This is possible by implementation of the the inversely adjusted optimal charge curve illustrated in Figure 3a, where the higher natural rate of growth commensurates with the lower applied voltage. In fact, the velocity of the growing dendrites $\dot{\lambda}$ has been utilized as a negative feedback for preventing the runaway dynamics. Consequently, the uniform rate of growth has been obtained as shown in Figure 3b, where the lowest augmentation in the electric field $f(r_d)$, which is due to sharp edges, allows for longer lasting dendrites before short circuiting takes place. This factor indicates that the more flat the surface is, the higher the number of atoms that will be deposited. Although this factor $f(r_d)$ should increase with the increase in the interface curvature r_d during the simulation run, we fix its value in order to ensure a similar effect of the same order for both uniform and optimized charging patterns.

The numerical discretization has been visualized in Figure 5. The ascribed visualizations from Figure 4 verifies the success in the applied optimal voltage pattern for the suppression of the dendrites, particularly relative to the uniform charge method. It is important to mention that the constant assumption of the spatial density ρ in Equation 1 makes it a controlled evolution during the analytical approach for equivalent deposited charge, while the reality is stochastic based, which is associated with the increasing density in time, making the feeding charge more in the beginning (with

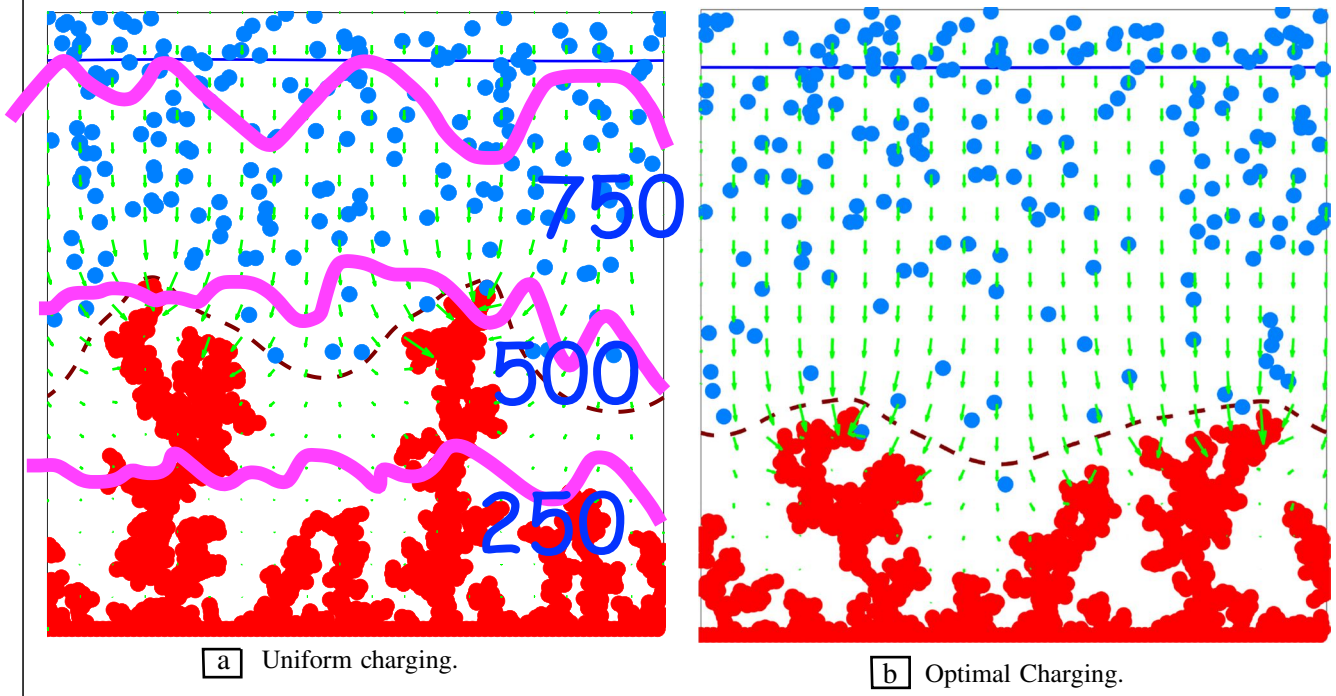

Figure 4. Comparing the resulted morphologies based on uniform and optimal charging patterns.

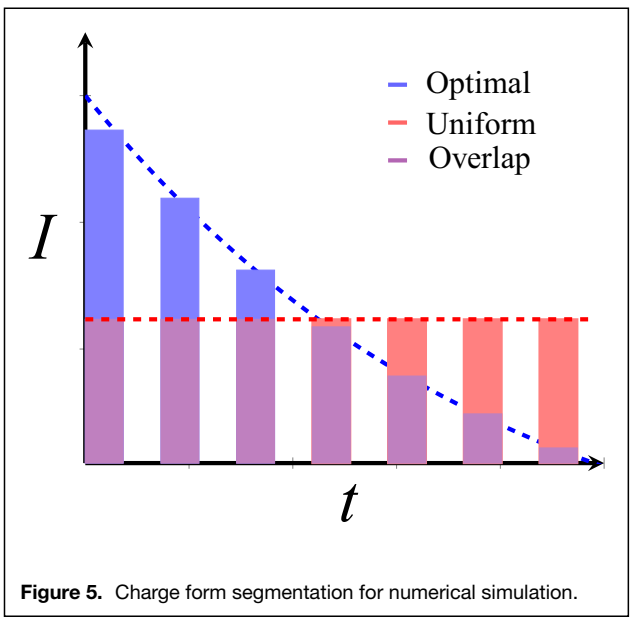

Figure 5. Charge form segmentation for numerical simulation.

highest density, *lowest rate of growth*) and less at the end (with *lowest density*, *highest rate of growth*).

Furthermore, Figure 6 illustrates that the optimal charge curve is additionally successful for a broader range of the charge values relative to uniform charge, leading to more packed density. The dendritic compression is ≈ %16 based on the simulation parameters (Table II). The difference in the range of the simulation and experimental values in this graph is due to feasibility of the computational power in the simulations (~ 100 ions $\sim 10^{-17}C$) versus the experimental charging scales ($\sim 10^{2}C$) albeit the density trends are in agreement when charging forms are compared.

Consequently, the short circuit time is extended due to formation of more packed morphology, which is also in agreement with Figure 3b in terms of extending the deposition time. Although applying the rest period relaxes the dendrites as well, it has been applied in similar manner for both charging methods and therefore the density difference is solely due to the applied charging form.

Table III. Numbers approximated for uniform and optimal charging.

Uniform	10	10	–	10	10	–	10	10
Optimal	40	21	–	4	3	–	1	0

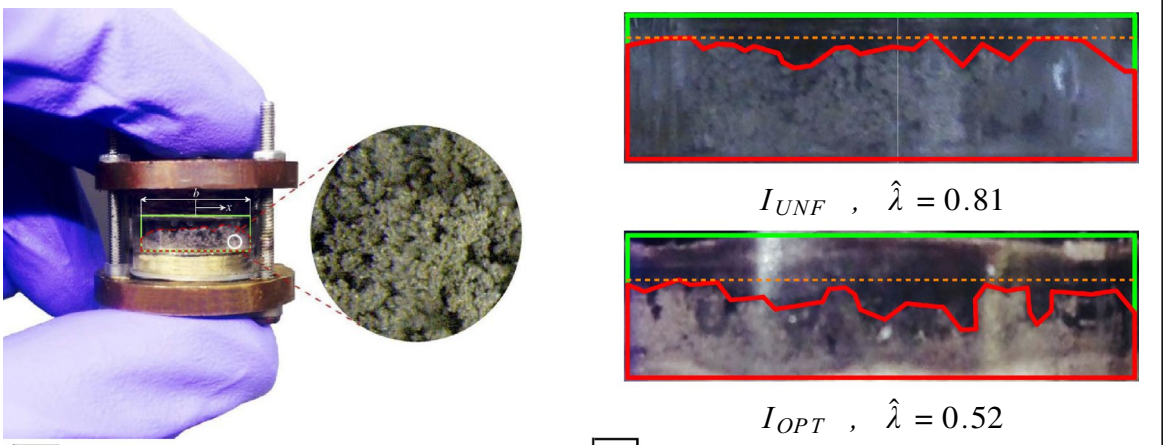

a Naked-eye observation of grown dendrites.[58]

b Sample of obtained morphologies for i_{OPT} (top) and i_{UNF} (bottom).

Figure 6. Obtained density of morphologies vs number of deposited atoms for optimal and uniform charging forms in both simulation (left) and experimental (right) results.

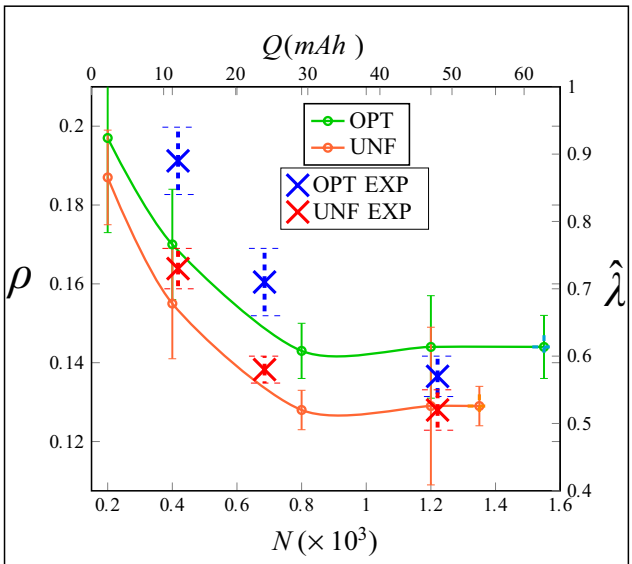

Figure 7. Experimental procedure.

It is important to note from Equation 12 that based on the analytical comparison, the presented charge form should provide the same height as the uniform charging. However the *stochastic* nature of the ionic deposition provides a shorter amount since the random propagation of the branches has *accelerating* behavior (ever-increasing porosity) based on the state of the branch. Therefore the best suppression occurs when the branches are in the very initial stage of growth and the highest amount of the charge could get fed to the dendrite. Vice versa, the excessive growth of the branches requires real-time restricted feeding charge due to instantaneous runaway state of the growth.

Needless to mention that although the simulation results are based on the charge amount, correlating with the applied current I and the analytical development is based on the voltage V, both are directly correlated with the Ohm's Law (i.e., scaling with the same magnitude) and the comparison is still valid.

Conclusion

In this article, we have developed a new real-time charge supply method for the compression of dendrites during electrodeposition. Tracking the runaway natural evolution dynamics of the microstructures, we tune the supply charge rate inversely to the natural growth rate hindering the excessive stochastic branching. Opposite to the rate of dendritic branching, the counter-rate charge would have a descending pattern in time as we have proven analytically. We have also analytically verified that in optimal case scenario, this technique leads to a constant growing speed of the morphology.

Performing the MD coarse grained simulation for the electrodeposits we have computationally shown that the optimized charge form did in fact generate a denser medium (i.e., less porosity) versus uniform charging, resulting in a smoother surface. This has been related to the stochastic nature of the

Table IV. Experimental parameters.

Parameter	Q	$t_{ON}(t)$	t_{OFF}	i_{max}	i_{min}	i_{UNF}	L	R	T	C_∞
Value	{12, 24, 48}	1	1	2	0	1	3.175	7.95	298	1
Unit	mAh	ms	ms	mA cm^{-2}	mAcm^{-2}	mA cm^{-2}	mm	mm	K	M

electrodeposition containing more attributes for excessive branching than the analytical approach with organized porosity distribution. In practice, the developed charging form could be programmed into a smart charger for portables and other chargeable devices.

Acknowledgments

The authors would like to thank and acknowledge the financial support from the Masri Institute (Award No. 103919) and University Research Board (Award No. 103950) at American University of Beirut.

References

1. S. Suzuki, H. Okada, K. Yabumoto, S. Matsuda, Y. Mima, N. Kimura, K. Kimura, arXiv preprint. arXiv:2010.04489 (2020)
2. W.H. Sim, H.M. Jeong, *Adv. Sci.* **8**(1), 2002144 (2021)
3. X. Xu, Y. Liu, J.-Y. Hwang, O.O. Kapitanova, Z. Song, Y.-K. Sun, A. Matic, S. Xiong, *Adv. Energy Mater.* **10**(44), 2002390 (2020)
4. M. Selvapandiyan, G. Balaji, N. Sivakumar, M. Prasath, S. Sagadevan, *Chem. Phys. Lett.* **762**, 138118 (2021)
5. Y. Wang, H.-Q. Sang, W. Zhang, Y. Qi, R.-X. He, B. Chen, W. Sun, X.-Z. Zhao, D. Fu, Y. Liu, *ACS Appl. Mater. Interfaces* **12**(46), 51563 (2020)
6. T. Gao, C. Rainey, W. Lu, *ACS Appl. Mater. Interfaces* **12**(46), 51448 (2020)
7. A. Ramasubramanian, V. Yurkiv, T. Foroozan, M. Ragone, R. Shahbazian-Yassar, F. Mashayek, *ACS Appl. Energy Mater.* **3**(11), 10560 (2020)
8. J. Qian, S. Wang, Y. Li, M. Zhang, F. Wang, Y. Zhao, Q. Sun, L. Li, F. Wu, R. Chen, *Adv. Funct. Mater.* **31**(7), 2006950 (2020)
9. Q. Yan, G. Whang, Z. Wei, S.-T. Ko, P. Sautet, S.H. Tolbert, B.S. Dunn, J. Luo, *Appl. Phys. Lett.* **117**(8), 080504 (2020)
10. D. Tewari, S.P. Rangarajan, P.B. Balbuena, Y. Barsukov, P.P. Mukherjee, *J. Phys. Chem. C* **124**(12), 6502 (2020)
11. C.-T. Yang, Y.-X. Lin, B. Li, X. Xiao, Y. Qi, *ACS Appl. Mater. Interfaces* **12**(45), 51007 (2020)
12. S. Sheng, L. Sheng, L. Wang, N. Piao, X. He, *J. Power Sources* **476**, 228749 (2020)
13. T. Witten, L.M. Sander, *Phys. Rev. B* **27**(9), 5686 (1983)
14. M. Matsushita, K. Honda, H. Toyoki, Y. Hayakawa, H. Kondo, *J. Phys. Soc. Jpn.* **55**(8), 2618 (1986)
15. J. Kertész, T. Vicsek, *J. Phys. A Math. Gen.* **19**(5), L257 (1986)
16. J.N. Chazalviel, *Phys. Rev. A* **42**(12), 7355 (1990)
17. V. Fleury, *Nature* **390**(6656), 145 (1997)
18. M. Rosso, T. Gobron, C. Brissot, J.-N. Chazalviel, S. Lascaud, *J. Power Sources* **97**, 804 (2001)
19. C. Monroe, J. Newman, *J. Electrochem. Soc.* **150**(10), A1377 (2003)
20. R. Akolkar, *J. Power Sources* **232**, 23 (2013)
21. D. Tewari, P.P. Mukherjee, *J. Mater. Chem. A* **7**(9), 4668 (2019)
22. A. Aryanfar, D. Brooks, B.V. Merinov, W.A. Goddard III, A. Colussi, M.R. Hoffmann, *J. Phys. Chem. Lett.* **5**(10), 1721 (2014)
23. W. Mu, X. Liu, Z. Wen, L. Liu, *J. Energy Storage* **26**, 100921 (2019)
24. D.R. Ely, A. Jana, R.E. García, *J. Power Sources* **272**, 581 (2014)
25. D.A. Cogswell, *Phys. Rev. E* **92**(1), 011301 (2015)
26. R. Akolkar, *J. Power Sources* **246**, 84 (2014)
27. Z. Ahmad, Z. Hong, Venkatasubramanian Viswanathan, *Proc. Natl Acad. Sci. U.S.A.* **117**(43), 26672–26680 (2020)
28. W. Huang, P. Feng, C. Gao, X. Shuai, T. Xiao, C. Shuai, S. Peng, *Int. J. Polym. Sci.* **2015**, 132965 (2015)
29. B. Moorthy, R. Ponraj, J.H. Yun, J.E. Wang, D.J. Kim, D.K. Kim, *ACS Appl. Energy Mater.* **3**(11), 11053 (2020)
30. T. Gao, C. Rainey, W. Lu, *ACS Appl. Mater. Interfaces* **12**(46), 51448(2020)
31. R. Wang, J. Yu, J. Tang, R. Meng, L.F. Nazar, L. Huang, X. Liang, *Energy Storage Mater.* **32**, 178 (2020)
32. W. Xu, J.L. Wang, F. Ding, X.L. Chen, E. Nasybutin, Y.H. Zhang, J.G. Zhang, *Energy Environ. Sci.* **7**(2), 513 (2014)
33. Z. Li, J. Huang, B.Y. Liaw, V. Metzler, J. Zhang, *J. Power Sources* **254**, 168 (2014)
34. Y. Ren, Y. Shen, Y. Lin, C.-W. Nan, *Electrochem. Commun.* **57**, 27(2015)
35. H. Lee, N. Sitapure, S. Hwang, J.S.-I. Kwon, *Comput. Chem. Eng.* **153**, 107415 (2021)
36. N. Schweikert, A. Hofmann, M. Schulz, M. Scheuermann, S.T. Boles, T. Hanemann, H. Hahn, S. Indris, *J. Power Sources* **228**, 237 (2013)
37. R. Younesi, G.M. Veith, P. Johansson, K. Edström, T. Vegge, *Energy Environ. Sci.* **8**(7), 1905 (2015)
38. M. Zhou, R. Liu, D. Jia, Y. Cui, Q. Liu, S. Liu, D. Wu, *Adv. Mater.* **33**(29), 2100943 (2021)
39. C.P. Nielsen, H. Bruus, arXiv preprint. arXiv:1505.07571 (2015)
40. P.P. Natsiavas, K. Weinberg, D. Rosato, M. Ortiz, *J. Mech. Phys. Solids* **95**, 92 (2016)
41. A. Aryanfar, T. Cheng, A.J. Colussi, B.V. Merinov, W.A. Goddard III, M.R. Hoffmann, *J. Chem. Phys.* **143**(13), 134701 (2015)
42. A. Aryanfar, D.J. Brooks, A.J. Colussi, B.V. Merinov, W.A. Goddard III, M.R. Hoffmann, *Phys. Chem. Chem. Phys.* **17**(12), 8000 (2015)
43. Y. Fan, Z. Wang, T. Fu, *Appl. Therm. Eng.* **199**, 117541 (2021)
44. A.W. Abboud, E.J. Dufek, B. Liaw, *J. Electrochem. Soc.* **166**(4), A667 (2019)
45. S. Chandrashekar, O. Oparaji, G. Yang, D. Hallinan, *J. Electrochem. Soc.* **163**(14), A2988 (2016)
46. A. Aryanfar, D.J. Brooks, W.A. Goddard, *MRS Adv.* **3**(22), 1201 (2018)
47. X. Zhang, Q.J. Wang, K.L. Harrison, K. Jungjohann, B.L. Boyce, S.A. Roberts, P.M. Attia, S.J. Harris, *J. Electrochem. Soc.* **166**(15), A3639 (2019)
48. C. Monroe, J. Newman, *J. Electrochem. Soc.* **151**(6), A880 (2004)
49. M. Klinsmann, F.E. Hildebrand, M. Ganser, R.M. McMeeking, *J. Power Sources* **442**, 227226 (2019)
50. G. Liu, D. Wang, J. Zhang, A. Kim, W. Lu, *ACS Mater. Lett.***1**(5), 498 (2019)
51. P. Wang, W. Qu, W.-L. Song, H. Chen, R. Chen, D. Fang, *Adv. Funct. Mater.* **29**(27), 1900950 (2019)
52. R. Bhattacharyya, B. Key, H. Chen, A.S. Best, A.F. Hollenkamp, C.P. Grey, *Nat. Mater.* **9**(6), 504 (2010)
53. S. Chandrashekar, N.M. Trease, H.J. Chang, L.-S. Du, C.P. Grey, A. Jerschow, *Nat. Mater.* **11**(4), 311 (2012)
54. Y. Li, Y. Qi, *Energy Environ. Sci.* **12**, 1286 (2019)
55. L.M. Kasmaee, A. Aryanfar, Z. Chikneyan, M.R. Hoffmann, A.J. Colussi, *Chem. Phys. Lett.* **661**, 65 (2016)
56. G. Yoon, S. Moon, G. Ceder, K. Kang, *Chem. Mater.* **30**(19), 6769 (2018)
57. M.Z. Mayers, J.W. Kaminski, T.F. Miller III, *J. Phys. Chem. C* **116**(50), 26214 (2012)
58. A. Aryanfar, Y. Ghamlouche, W.A. Goddard III, *Electrochim. Acta* **367**, 137469 (2021)
59. M.Z. Bazant, B.D. Storey, A.A. Kornyshev, *Phys. Rev. Lett.* **106**(4), 046102 (2011)
60. A. Aryanfar, Y. Ghamlouche, W.A. Goddard III, *J. Chem. Phys.* **154**(19), 194702 (2021)
61. R. Koerver, W. Zhang, L. de Biasi, S. Schweidler, A.O. Kondrakov, S. Kolling, T. Brezesinski, P. Hartmann, W.G. Zeier, J. Janek, *Energy Environ. Sci.* **11**(8), 2142 (2018)
62. K. Nishikawa, Y. Fukunaka, T. Sakka, Y.H. Ogata, J.R. Selman, *J. Electrochem. Soc.* **153**(5), A830 (2006)
63. J.-H. Kim, N.P.W. Pieczonka, L. Yang, *ChemPhysChem* **15**(10), 1940 (2014)
64. B.N. Taylor, A. Thompson, *The International System of Units (SI).* International Bureau of Weights and Measures Publication (US Department of Commerce, Technology Administration, National Institute of Standards and Technology, 2001)
65. A. Aryanfar, Y. Ghamlouche, W.A. Goddard III, *Phys. Rev. E* **100**(4), 042801 (2019)
66. J. Philibert, *Diffus. Fundam.* **4**(6), 1 (2006)
67. R.A. Serway, J.W. Jewett, *Physics for Scientists and Engineers* (Cengage Learning, Boston, 2018)
68. A. Aryanfar, US Patent 9,620,808 (April 11, 2017)
69. N. Otsu, *Automatica* **11**(285–296), 23 (1975)
70. A. Aryanfar, D.J. Brooks, A.J. Colussi, M.R. Hoffmann, *Phys. Chem. Chem. Phys.* **16**(45), 24965 (2014) □